UNIVERSITY OF LEOBEN
DEPARTMENT OF MATERIALS PHYSICS

Comparative study on the miscibility of Cu-Fe-Co compounds processed by methods of severe deformation

Bachelor Thesis

Kasalo Manoel

Leoben, September 2019

Affidavit

I declare in lieu of oath, that I wrote this thesis and performed the associated research myself, using only literature cited in this volume.

Leoben, September 2019	
Place, Date	Kasalo Manoel

Abstract

This thesis deals with investigations regarding the microstructural development of severe plastically deformed samples by high-pressure torsion of the ternary system Cu-Fe-Co, whereby the individual components (besides Co-Fe) are immiscible at the thermodynamic equilibrium. Two various compositions, $Cu_{20}(Fe_{70}Co_{30})_{80}$ and $Cu_{20}(Fe_{15}Co_{85})_{80}$, were fabricated out of elemental powders, then deformed by high-pressure torsion and exposed to subsequent conventional annealing treatments. The obtained microstructures were compared by using light microscopy, scanning electron microscopy, X-Ray diffraction and Vickers hardness measurements. A single-phase microstructure could be reached for $Cu_{20}(Fe_{15}Co_{85})_{80}$. In contrast to that, the Fe-rich samples exhibit residual particles embedded in a supersaturated matrix. The resulting microstructure consists therefore of two phases. An enhancement of intermixing was achieved with powder mixtures, which were pre-treated by ball milling and subsequently deformed by high-pressure torsion. Ball milling, however, led to brittle samples which exhibit more cracks. Nevertheless, grain sizes in the nanocrystalline regime were obtained for all as-deformed samples. Furthermore, conventional annealing led to a homogenous microstructure and grain coarsening in each case. In comparison, the as-deformed and annealed $Cu_{20}(Fe_{15}Co_{85})_{80}$ samples exhibit a higher thermal stability.

Contents

Abbrevations

HPT	high-pressure torsion
SPD	severe plastic deformation
BM	ball milling
SEM	scanning electron microscopy
BSE	back scattered electrons
XRD	X-ray diffraction
UFG	ultrafine grained
NC	nanocrystalline
ECAP	equal channel angular pressing
ARB	accumulative roll bonding
CA	conventional annealing
LM	light microscopy
HV	Vickers hardness
RT	room temperature
EDX	energy dispersive X-ray spectroscopy
FWHM	full width at half maximum

1 Introduction

1.1 Motivation

It has been known for more than 30 years, that materials with good soft magnetic properties, i.e. coercivity below 1000 A/m, require very large grains (>100µm). The coercivity increases with decreasing grain size. Thus, materials with small grain sizes have been considered only as hard magnetic materials (i.e. exhibit large coercivity). However, in the late 1980s, soft magnetic properties were also observed for the nanocrystalline (NC) regime (<20 nm). This means, soft and hard magnetic behavior can be closely neighbored for materials with a fine microstructure. Soft magnetic materials are used for power supply transformers, relays, pole shoes and magnetic shielding. To synthesize homogeneous nanostructured materials, several methods are used, such as vapor quenching method or magnetron sputtering [1], [2]. Rapid solidification from the liquid state, namely melt spinning, is applied for large scale production. The grain size, and therefore coercivity can be tuned by subsequent annealing treatments. Because samples are prepared as ribbons, it is necessary to produce applicable magnets by additional work stages, e.g. tape wounding. One may overcome such issues by using top-down techniques, i.e. to produce nanostructured samples directly in bulk form.

For this purpose, high-pressure torsion (HPT) can be used. HPT is a technique of severe plastic deformation (SPD), where a continuous and arbitrary amount of shear strain can be applied, leading directly to samples in bulk form. Furthermore, by blending of elemental powders followed by compaction of the powder mixture, a wide range of various compositions is accessible. This technique was already used to observe the magnetic properties of binary solid solutions, e.g. Co-Cu, which are immiscible at the thermodynamic equilibrium. Recent studies showed, that these samples possess intermixed phases consisting of ferromagnetic and diamagnetic components. Co-Cu alloys showed a low coercive field strength, which can be explained by random anisotropy [3], [4].

In comparison to Co, Fe exhibits an enhanced magnetic moment. Therefore, to tune the magnetic moment, while obtaining low coercivity, a partial substitution of Co with Fe is investigated in this thesis. In particular, two various compositions, $Cu_{20}(Fe_{70}Co_{30})_{80}$ and $Cu_{20}(Fe_{15}Co_{85})_{80}$, are investigated. Anyway, the focus herein is on the synthetization of samples, as well as on the evolution of the microstructure. The immiscible elemental powders, diamagnetic pure Cu and ferromagnetic Fe-Co alloys are prepared by ball milling (BM) and HPT. The microstructure of the as-deformed and annealed samples are characterized by scanning electron microscopy (SEM) and X-Ray diffraction (XRD).

1.2 Investigated systems

The three binary phase systems Co-Cu, Co-Fe and Fe-Cu are mapped in Figure 1 (a), (b) [5] and (c) [6]. As can be seen, Co and Fe are miscible, hence Co-Fe alloys can be formed for a wide range of compositions under equilibrium conditions. The mutual solubility of Cu-Fe and Cu-Co System decreases for decreasing temperatures and becomes vanishingly low at room temperature (RT). Nonetheless, J. Eckert et. al. successfully prepared supersaturated NC Fe_xCu_{1-x} alloys by BM, whereby single-phase fcc structure with x<0.6 and bcc structure with x>0.8 have been formed. Between that values both phases coexist.
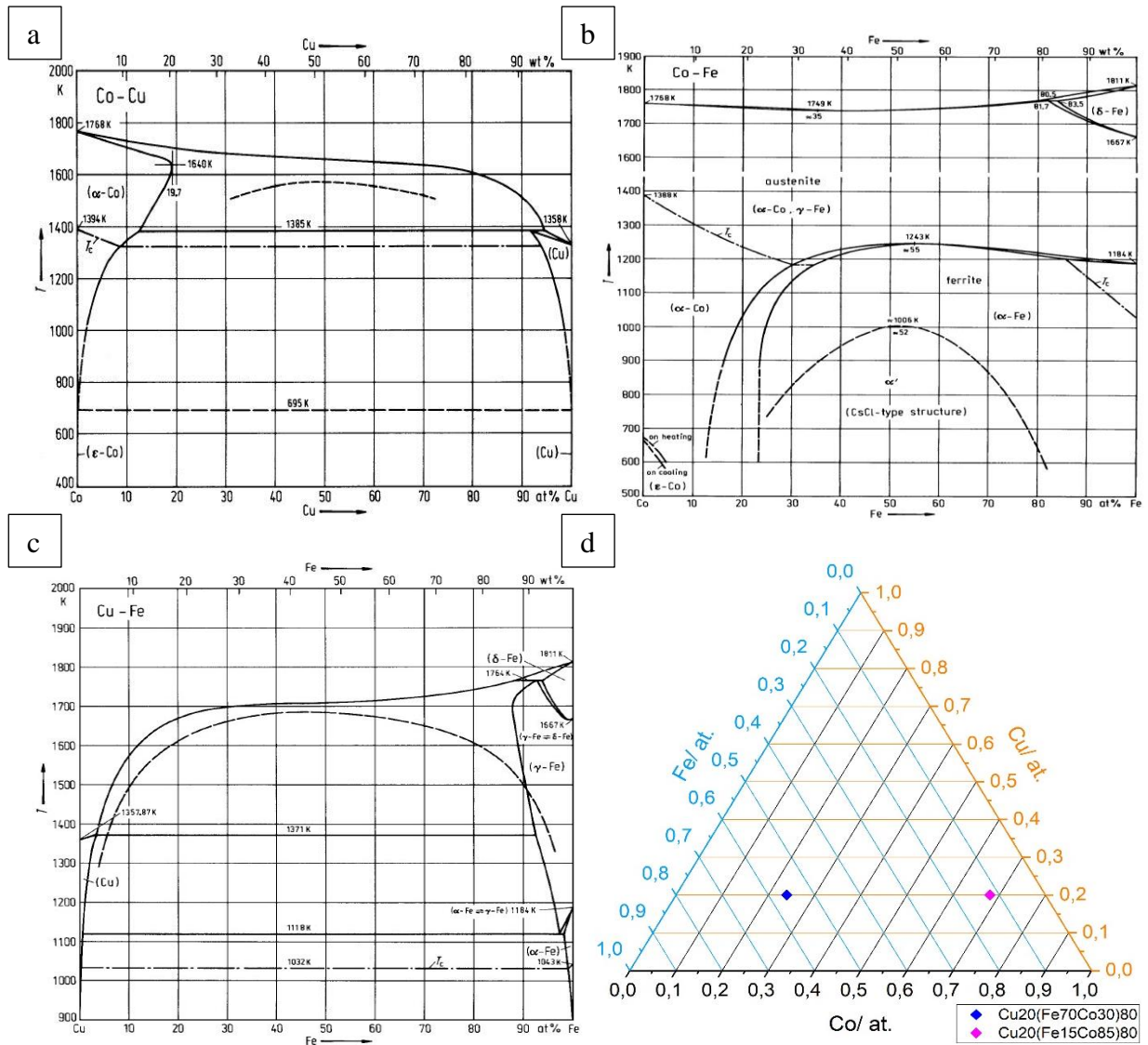

Figure 1: (a) Co-Cu binary phase diagram. The dashed line indicates the metastable miscibility gap in the liquid state [5]. (b) Co-Fe binary phase diagram. The dashed lines indicate the metastable miscibility gap in the solid state [5]. (c) Cu-Fe binary phase diagram. The Curie temperature Tc is indicated by the dashed-dotted line. The dashed line provides the metastable miscibility gap for supercooled liquid alloys [6]. (d) Cu-Co-Fe ternary phase diagram with investigated compositions $Cu_{20}(Fe_{70}Co_{30})_{80}$ and $Cu_{20}(Fe_{15}Co_{85})_{80}$.

In contrast, BM-treated Co-Cu powders exhibit for all compositions a single-phase fcc structure [7]. It has already been shown, that HPT can also be used to produce supersaturated solid solutions out of the immiscible systems Co-Cu and Fe-Cu [4]. A magnetoresistive granular alloy of $Cu_{80}(Fe_{70}Co_{30})_{20}$ can be produced by various BM processes. One of them starts with milling a stochiometric mixture of the pure powders. The result is an inhomogeneous distribution of Co and Fe in the Cu matrix. By a subsequent annealing treatment, the desired composition, a Cu matrix with nano dispersed $Fe_{70}Co_{30}$ clusters, was obtained [8]. However, only the production of powders is possible by BM, for this purpose HPT can be used to form bulk samples. In this study two different compositions of a ternary Cu-Co-Fe system are investigated, $Cu_{20}(Fe_{70}Co_{30})_{80}$ and $Cu_{20}(Fe_{15}Co_{85})_{80}$, which are shown in Figure 1 (d).

1.3 Ball Milling

BM is a solid-state processing method to synthesize homogenous nanostructured granular alloys of blended powders. During high-energy BM, the powder particles collide repeatedly with grinding balls, whereby the particles are plastically deformed, fractured and cold welded. The main benefits of BM are:

- Significant decrease in grain size (nanometer regime)
- Extension of solid solubility
- Formation of agglomerated powder particles [9]
- Generation of various equilibrium and non-equilibrium alloy phases, such as supersaturated solid solutions [10]

The major disadvantage of BM is that the obtained material is in powder form, therefore a further powder compaction process is necessary to achieve a bulk sample. Additionally, a mixture of an alloy consisting of one or more low-melting elements is difficult to produce because of high local temperatures during the collision of grinding balls. Another disadvantage of BM is, that a contamination of material is possible because of abrasion of the grinding balls. Furthermore, the process parameters during BM cannot be controlled precisely compared to HPT, such as the applied strain or strain rate.

1.4 High-pressure torsion

In the last 30 years different SPD techniques, such as HPT, have been developed and improved to fabricate ultrafine grained (UFG) (1 - 2 µm), submicron (100 nm - 1 µm) and even NC (< 100 nm) bulk materials [11],[12]. By applying very high strains on coarse grained materials, a strong and uniform grain refinement can be achieved, which can lead to improved mechanical

and physical properties. The structural evolution of SPD deformed materials at large strains is strongly dependent on various processing parameters, e.g. temperature, pressure, strain rate, strain path (monotonic or cyclic shear deformation) and alloying [13], [14].

The ideal HPT process is a shear process. The shear strain γ can be evaluated as shown in Equation 1, assuming a constant specimen thickness.

$$\gamma = \frac{2\pi \cdot r}{t} \cdot n \tag{1}$$

In Equation 1, n is the number of revolutions, r denotes the radius and t the thickness of the specimen. Anyway, to compare the strain to other deformation processes, e.g. a tensile test, the von Mises equivalent strain ε can be calculated according to Equation 2:

$$\varepsilon = \frac{\gamma}{\sqrt{3}} \tag{2}$$

The shear strain exhibits a linear dependence on the radius, i.e. should be zero in the center and highest at the edge of the sample, in the case of ideal torsion deformation. However, during the real HPT process the sample thickness decreases due to plastic flow of the material, therefore Equations 1 and 2 are applicable if the thickness to diameter ratio, t/d, is smaller than 1/10. In addition, the above-mentioned equations are not valid in the immediate vicinity of the edge of the specimen [11].

A schematic illustration of HPT is depicted in Figure 2 (a) [13]. A disc shaped specimen is placed between two anvils, each of both has a cylindrical, slightly conical cavity. The cavities of the anvils must be fully filled with the sample material, and therefore the sum of both cavity heights should be somewhat smaller than the sample height. The anvils are pressed together and then rotated against each other. In order to accomplish plastic deformation, the sample material must flow into the small slit between the anvil pairs to avoid contact between anvils, and furthermore, to prevent sliding between anvils and sample material, a certain pressure is necessary (several GPa). For this purpose, the applied pressure should be about at least three times the yield stress of the undeformed sample material. Furthermore, the maximum pressure is limited by the yield stress (about three times) of the anvils [14]. Samples can be processed at various temperatures, by cooling or heating the anvils during deformation. Inserting an induction heating coil allows processing temperatures up to approximately 500°C while using liquid nitrogen permits temperatures down to -196°C. A simple way of changing the process parameters is useful for investigations of their influence on the microstructural development. Furthermore, using strain gauges enables a direct torque measurement during HPT, which can be used to estimate the change of the flow stress in-situ. As shown in Figure 2 (b), axial, radial and tangential are those directions, in which the sample is usually observed.
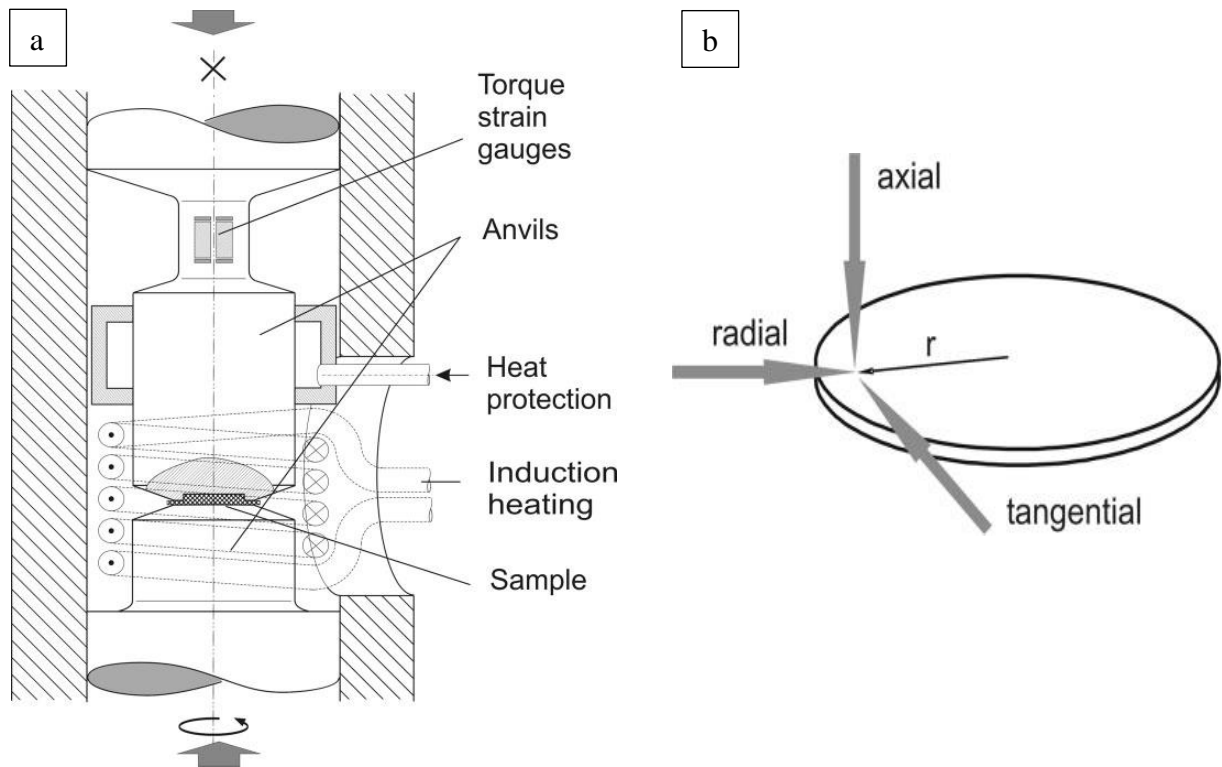
4

Figure 2: Schematic illustration of (a) the HPT equipment and (b) disc shaped HPT specimen showing different observation directions [13].

The main benefit of HPT, due to continuous deformation is that very high values of shear strain can be obtained easily, which cannot be achieved by another SPD techniques such as equal channel angular pressing (ECAP) or accumulative roll bonding (ARB). For example, a sample of a thickness of 0.8 mm deformed with one revolution corresponds to an equivalent shear strain of approximately 16, whereas 100 revolutions are equivalent to 1600 at a radius of 3.5 mm. Furthermore, HPT allows SPD at low temperatures (at which severe deformation often is impossible for other SPD techniques) of relatively brittle or high-strength materials. Because of extended hydrostatic pressure, crack formation can be prevented [11], [13]. An upscaling of sample size is also possible by using bigger anvils and a HPT device which allows an application of higher forces and torques. Moreover, HPT can even be applied to consolidate powder mixtures so that the obtained bulk sample can be deformed subsequently.

The major disadvantage of HPT is that a uniform application of the shear strain is not possible due to radial dependency. Moreover, HPT cannot be used for a large scale production of bulk nanocomposites, in contrast to ARB [13].

1.4.1 Deformation of single-phase and multiphase materials

During SPD of single-phase materials, the dislocation density increases dramatically with increasing strain. These dislocations arrange themselves as grain boundaries, which subdivide the initial grains into cell blocks with large misorientations as well as into ordinary dislocation cells with smaller misorientations. With increasing strain, the sizes of the cells decrease and the misorientations of neighboring cells increase, which leads to a transformation of the cells to an uniform granular structure [13], [15]. However, an infinitely high strain does not lead to infinitesimal small grains. A saturation of this refinement process has been observed for many pure metals and alloys, i.e. a minimum of crystallite size is achieved by applying a critical strain and the size cannot be further reduced by increasing strain. Thus, increasing strain lead to a steady state in microstructure and hardening. This saturation profile is schematically illustrated in Figure 3 [13].
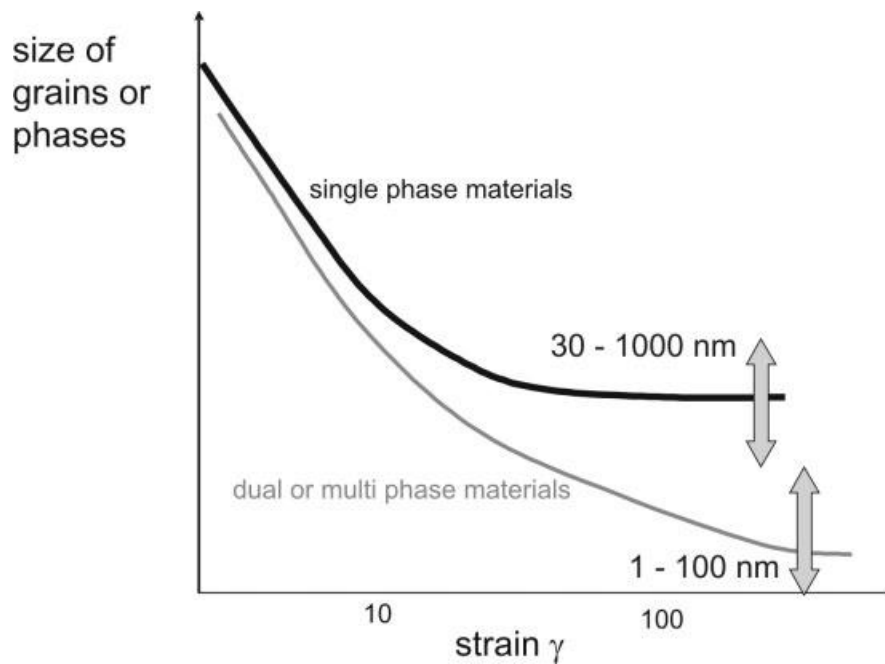
Figure 3: Schematic illustration of the structural refinement of single- and dual- or multiphase materials as a function of applied shear strain [13].

In general, the obtained minimum grain size of single-phase materials after SPD is affected by processing parameters, mainly dependent on strain, strain path and deformation temperature and only slightly dependent on strain rate and applied pressure. With increasing temperatures, crystallite size increases because of increasing grain boundary migration and triple junction motion [16]. Shear deformation and diffusion work against each other during HPT.

Furthermore, alloying has a strong influence on microstructure. As indicated in Figure 3, composite materials can achieve a smaller minimum grain size than single-phase materials,

although, higher strains are needed. HPT can even be used to produce supersaturated solid solutions out of typically immiscible materials. In general, the deformation behavior induced by SPD of multiphase materials is more complex than in single-phase materials. For example, a coarse- grained W-Cu composite (metal-metal composite) was deformed by HPT, whereby it was observed that the stronger and more brittle W phase fractures into NC particles. Another deformation behavior was observed for metal matrix composites, such as Al6061 - 10% SiC composite. In this case the embedded and harder particles were not deformed, but the clusters distributed homogenously in the soft matrix. Moreover, the formation of single- and dual-phase supersaturated solid solutions of different binary systems is also possible by HPT-deformation [4] even if the mutual solubility of the solid phases is vanishingly low at RT and equilibrium conditions.

2 Materials and Methods

Within the framework of this thesis, the production of two $Cu_{20}(Fe_xCo_{100-x})_{80}$ compositions and their microstructural development were examined. First, the stochiometric mixtures of the pure elemental metal powders, $x = 70$ % and $x = 15$ %, were mixed in a glove box in an inert argon atmosphere. The used elemental powders, their size range of particles and their manufacturer are listed in Table 1. SEM micrographs of the powders are displayed in the appendix.

Table 1: Parameters of used elemental metal powders with a purity of 99.9 %.

Powder Material	Min.-Max. Particle Size/µm	Manufacturer-Type
Co	50-150	Good Fellow -100+270 mesh
Cu	37-88	Alfa Aesar -170+400 mesh
Fe	74-149	MaTeck -100+200 mesh

Basically, both powder compositions were mixed and hydrostatically compacted in argon atmosphere. The powder composition $Cu_{20}(Fe_{70}Co_{30})_{80}$ was also prepared as a granular alloy by BM in addition to the conventional powder mixture. In more detail, $Cu_{20}(Fe_{70}Co_{30})_{80}$ was milled in a Retsch Planetary Ball Mill PM400 in argon atmosphere with a rotational speed of 300 rpm for 12h in total. The grinding balls to powder ratio was 10:1, whereby 20 g bigger and 80 g smaller steel balls were used. Investigation of the microstructural evolution of the BM process has been carried out with XRD (more about this below). For this purpose, a small amount of powder was removed after every two hours effective milling time. The rotational direction was reversed every 30 min with a break of 15 min in between to prevent temperature increase.

To obtain bulk samples, the powders were consolidated hydrostatically in an argon atmosphere. For this purpose, a Cu ring was placed between two steel anvils (each of both had a cavity height of 0.3 mm), concentric to their cavities. The powder mixture was filled in the hollow space, then the anvils were pressed with an applied pressure of 5 GPa and rotated against each other for 20 seconds with a rotational speed of 0.2 rpm. Bulk samples with 8 mm in diameter and an average height of 1.4 mm were fabricated by this method. For HPT deformation, the following processing parameters were used for each sample: an applied pressure of 5 GPa and a rotational speed of 1.28 rpm. Ball milled $Cu_{20}(Fe_{70}Co_{30})_{80}$ was processed by 5 revolutions at RT and by 10 revolutions at 300°C, 400°C and 500°C. Conventional powder mixtures $Cu_{20}(Fe_{70}Co_{30})_{80}$ and $Cu_{20}(Fe_{15}Co_{85})_{80}$ were processed by 50 revolutions at RT and 300°C. For HPT at RT, air cooling was used to prevent heating. Basically, for each anvil of a set, a cavity

height of 0.15 mm was chosen for processing at RT and 0.2 mm at higher temperatures, respectively. After HPT of the pre-compacted samples at above mentioned processing parameters, the resulting disc shaped specimen exhibited approximately 8 mm in diameter and 0.6 mm in height. For example, Table 2 show the calculated values of shear strain at given radii of un-milled $Cu_{20}(Fe_{15}Co_{85})_{80}$ deformed by HPT by 50 revolutions at RT. The values were estimated for a sample thickness $t = 0.41$ mm according to Equation (1).

Table 2: Resulting values of shear strain at different radii of $Cu_{20}(Fe_{15}Co_{85})_{80}$.

r / mm	0	1	2	3
γ / -	0	800	1500	2300

After HPT, all samples were cut by a water-cooled diamond wire, then one quarter of the sample was exposed to an isothermal conventional annealing treatment (CA) at 500°C for 1h in air atmosphere followed by a subsequent quenching in water. Thus, it was possible to compare both halves of the same sample in structure and hardness, one half was only in as-deformed condition, the second half was further annealed and investigated afterwards.

For preliminary investigations of the microstructure, an optical light microscope (LM) by Olympus BX51 was used. Due to the NC structure, a sufficient resolution could not be reached with a LM and thus it was only used to capture overview images. Additionally, a Zeiss Leo 1525 scanning electron microscope was used, which enables much higher resolutions than a LM. As schematically shown in Figure 4, both, reflected light of LM and scattered electron beam of SEM were detected in the tangential sample direction, whereby with regard to the latter a backscattered electrons (BSE) detector was used. Basically, SEM micrographs were taken with an acceleration voltage of 20 kV and an aperture size of 60 µm at the half of sample height at different radii (0 mm, 1 mm, 2 mm and 3 mm approximately). In this way, the development of the microstructure of an HPT deformed sample can be observed and correlated to the applied strain.

Microhardness (Vickers, HV) was measured using a Buehler Micromet 5100. The indenter (diamond pyramid) was pressed into the middle position of the cross-section surface parallel to the tangential direction. For each sample, as-deformed and annealed, indentations were taken along radii in steps of 0.25 mm over the entire cross-section with a constant load of 500 g (HV0.5), see Figure 4.
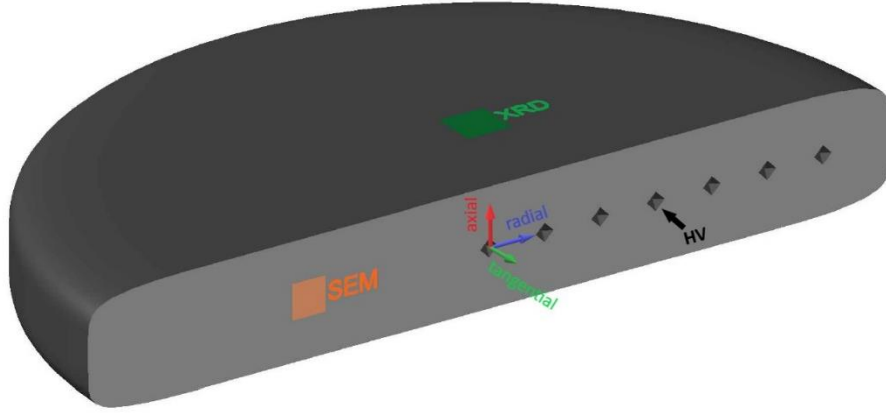
Figure 4: Schematic illustration of half of an HPT sample and positions where measurements were carried out.

To investigate the constituting crystalline phases, XRD measurements were carried out using a 1D detector. The angle between primary beam and sample surface, orthogonal to axial observation direction, remains θ and the angle between diffracted beam and transmitted primary beam is 2θ. The orientation in which the XRD patterns were taken is shown in Figure 4. The measurements were carried out by BRUKER D2 Phaser using Co-Kα radiation with a wavelength of $\lambda = 0.178897$ nm and a measuring range of $45° \leq 2\theta \leq 105°$ was set for each measurement. For enhanced statistical recording the sample was rotated with a rotational speed of 15 rpm and measured with 3000 steps and 3 seconds per step.

3 Results and discussion

3.1 Microhardness as function of applied strain

At first, the structural evolution of both Cu-Fe-Co compositions processed by HPT (50 revolutions) were studied. Therefore, the bulk samples were cut in half and polished for LM and microhardness measurements. An overview of the cross-section of the as-deformed samples can be seen in the LM images in Figure 5. The LM images a), b) and d) show a homogenous microstructure at radii bigger than ~1.5 mm and an inhomogeneous microstructure in the immediate vicinity of the center. A deformation is visible in the center of the sample, but not extensive enough. To verify that, a chemical phase analysis was carried out at this location by energy-dispersive X-Ray spectroscopy (EDX), which is shown in detail in the appendix. The sample in Figure 5 a) exhibits a bigger area of inhomogeneous deformation than those in b) and d), corresponding to samples deformed at 300°C. In comparison, the sample in c) shows an inhomogeneous microstructure in the entire sample. At the bottom and the middle of the sample, a high concentration of Cu can be observed. The reason for this is the difference in particle sizes (see Table 1). The small Cu particles move between the bigger Co and Fe particles and accumulate at the bottom of the sample before powder consolidation was carried out.
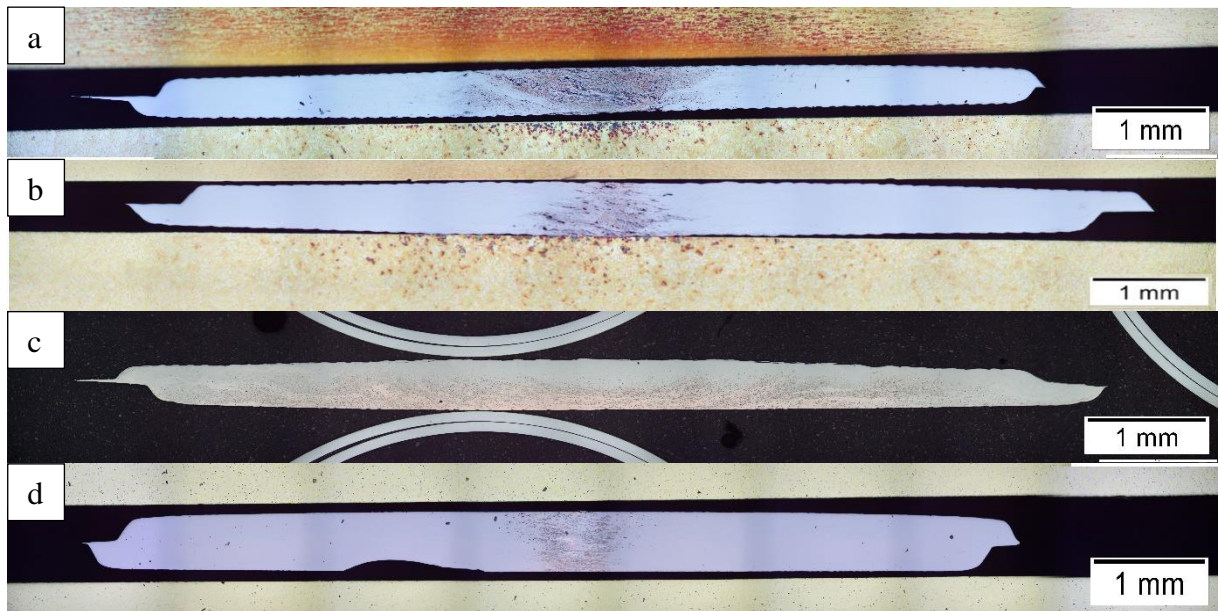
Figure 5: LM images of HPT deformed samples by 50 revolutions at different temperatures (samples fabricated out of conventional powders): a) $Cu_{20}Fe_{12}Co_{68}$ at RT b) $Cu_{20}Fe_{12}Co_{68}$ at 300°C c) $Cu_{20}Fe_{56}Co_{24}$ at RT d) $Cu_{20}Fe_{56}Co_{24}$ at 300°C.

Figure 6 show the results of Vickers hardness measurements as a function of applied strain of the investigated systems a) $Cu_{20}Fe_{12}Co_{68}$ and b) $Cu_{20}Fe_{56}Co_{24}$. The measurement was carried

out over the entire diameter for all samples, except the CA samples, where just one side of the sample could be considered. As can be seen in Figure 6, the hardness of all samples increases with increasing shear strain, which is proportional to the radius. However, hardness values show a saturation behavior at a specific value of shear strain, $\gamma \sim 1500$, which corresponds to a radius $r \geq 2\,$mm according to Equation 1. This invariable hardness suggests a steady state in microstructure for as-deformed samples above this position. The large decrease of hardness in the middle position of as-deformed $Cu_{20}Fe_{12}Co_{68}$ by 50 revolutions at RT in Figure 5 a) corresponds to the less deformed regions visible.

As mentioned in the beginning, an increase in HPT processing temperature leads to larger grain sizes in the steady state. The microhardness of materials is dependent on the grain size, in a similar way as the flow stress in the well-known Hall-Petch relationship [17]. An increase in grain size leads to a decrease in flow stress and therefore also to a decrease in hardness. As expected, in Figure 6 a) the sample deformed at RT shows a slight higher hardness level in the steady state, during in b) $Cu_{20}Fe_{56}Co_{24}$ exhibits a much smaller hardness level for deformation at RT. The difference in hardness is approximately 300 HV and the constant hardness profile can be explained with the LM image in Figure 5 c). An inhomogeneous elemental distribution can be observed, especially the Cu phase is arranged along the whole diameter, where also the indentations were carried out. Vickers hardness measurements are sensitive to small changes in the microstructure, so the softest element in the composition, Cu, causes lower hardness values for deformation at RT than at 300°C.
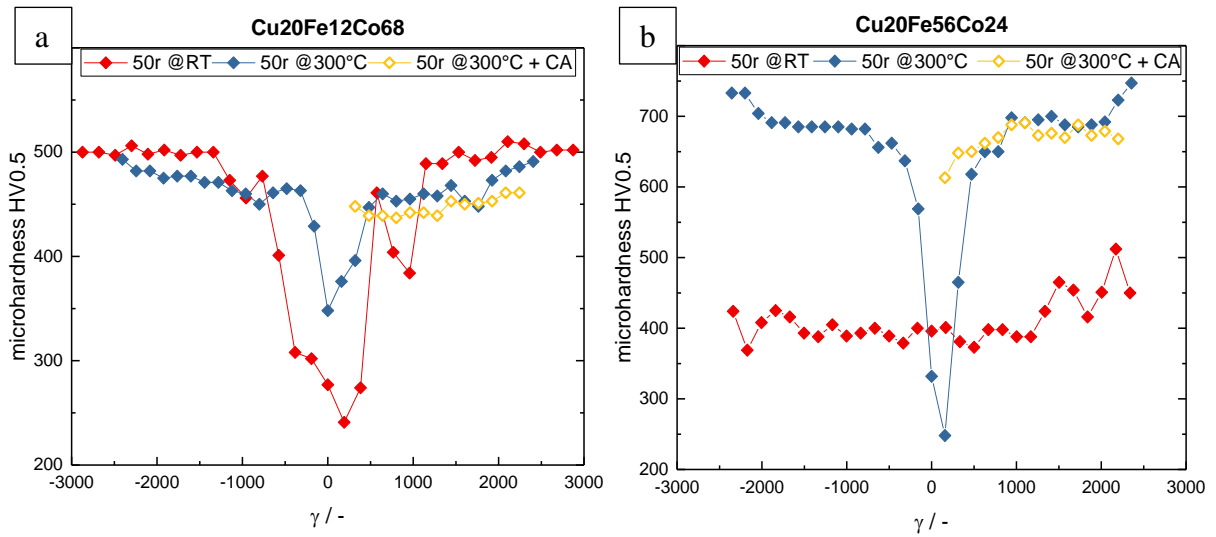
Figure 6: Vickers hardness as a function of applied strain of the investigated compositions processed by HPT.

For both compositions deformed at 300°C, a CA was carried out. The hardness after annealing is also shown in Figure 6. The annealing treatment had only a slight influence on microhardness, just a decrease of approximately 25 HV was observed for the CA samples in the saturation

regime. Basically, a comparison of both compositions deformed at 300°C shows that more Fe content leads to a higher hardness. A mean hardness for indentations above $r \geq 2$ mm of about 475 HV was measured for $Cu_{20}Fe_{12}Co_{68}$ and 700 HV for $Cu_{20}Fe_{56}Co_{24}$. In relation to the Vickers hardness of the undeformed individual elements, 608 MPa for Fe-bcc, 1043 MPa for Co-hcp and 369 MPa for Cu-fcc [18],the Co-rich sample is expected to have a higher microhardness.

3.2 Investigations of microstructural evolution using SEM

3.2.1 Microstructure as a function of shear strain

To investigate the microstructure on a smaller scale, investigations with SEM were carried out. Figure 7 a)-d) show SEM micrographs (back scattered electrons, BSE) of as-deformed $Cu_{20}Fe_{12}Co_{68}$ at a radius of 0, 1, 2 and 3 mm, carried out in tangential observation direction and same magnification. With increasing radii, the shear strain increases, therefore Figure 7 represents the microstructural development of the sample dependent on applied shear strain. The structural evolution of as-deformed $Cu_{20}Fe_{12}Co_{68}$ (50 revolutions at 300°C) is shown here as an example. Other samples have a similar behavior regarding the microstructural evolution and can be looked up in the appendix. The micrographs of a) and b) in Figure 7 show an inhomogeneous distribution of the elongated constituent phases, because of lower shear deformation with respect to c) and d). Above $r \geq 2$ mm, the micrographs indicate a fine homogeneous structure, which remains constant in respect of grain size and the phase distribution in spite of increasing shear strains. As a saturated state can be deduced from hardness measurements and SEM micrographs, in the further course, microstructural investigations are carried out at $r \geq 2$ mm as a steady state is reached.
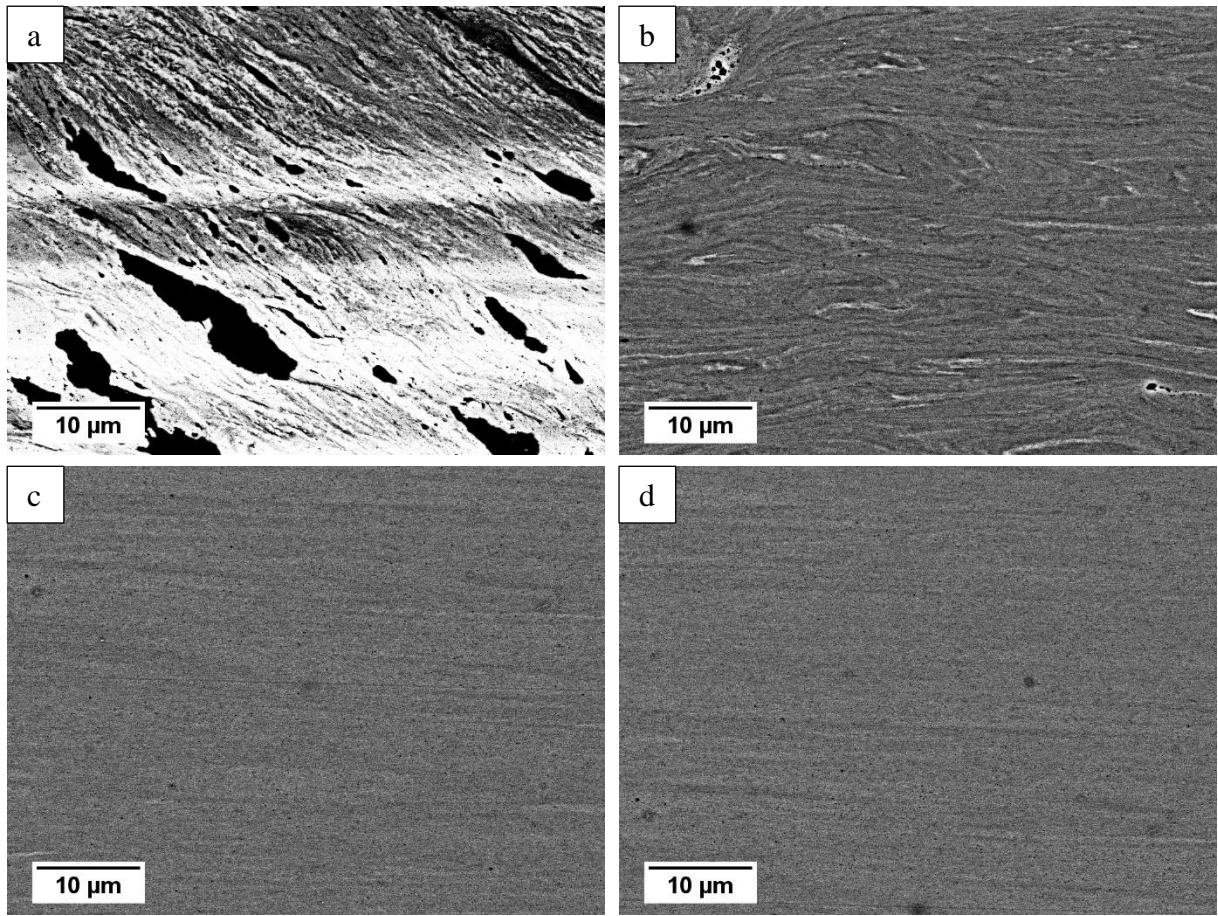
Figure 7: BSE micrographs of radial structural evolution of HPT deformed $Cu_{20}Fe_{12}Co_{68}$ sample (50 revolutions at 300°C) at: a) 0 mm b) 1 mm c) 2 mm and d) 3 mm. The shearing direction is parallel to the horizontal axis.

3.2.2 Influence of subsequent annealing on microstructure

To investigate the influence of a subsequent annealing on the microstructural evolution, SEM micrographs of as-deformed states are compared to CA states. The influence of CA after HPT deformation on the microstructure of $Cu_{20}Fe_{56}Co_{24}$ and $Cu_{20}Fe_{12}Co_{68}$ samples are shown in the micrographs in Figure 8 and Figure 9, respectively. In both figures, the micrograph in a) shows the respective as-deformed sample (50 revolutions at 300°C) and the micrograph in b) shows the same sample, exposed to an additional subsequent CA treatment.
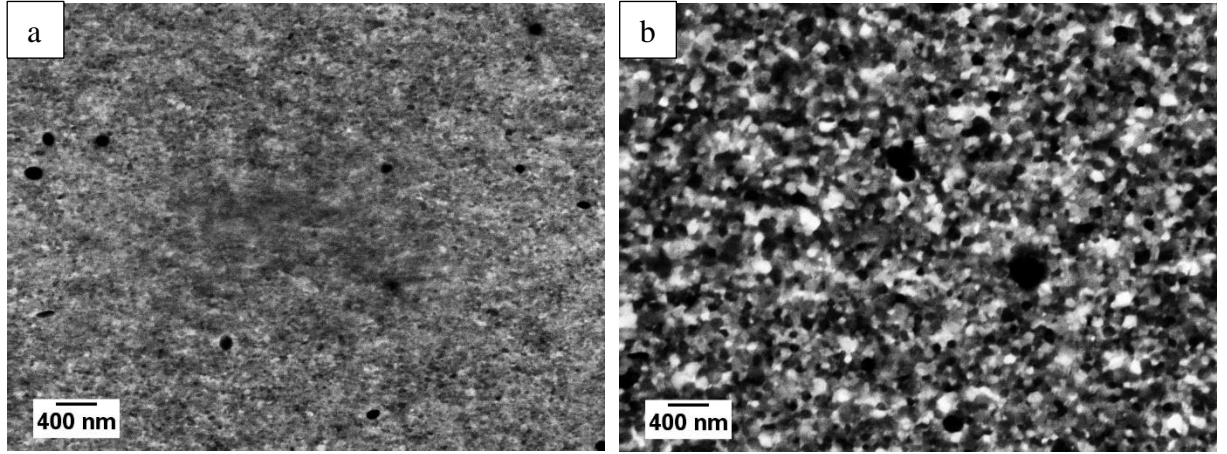
Figure 8: BSE micrographs of as-deformed $Cu_{20}Fe_{56}Co_{24}$ sample (50 revolutions at 300°C) taken at r = 3 mm: a) as-deformed b) as-deformed and CA (1h at 500°C). The shearing direction is parallel to the horizontal axis.
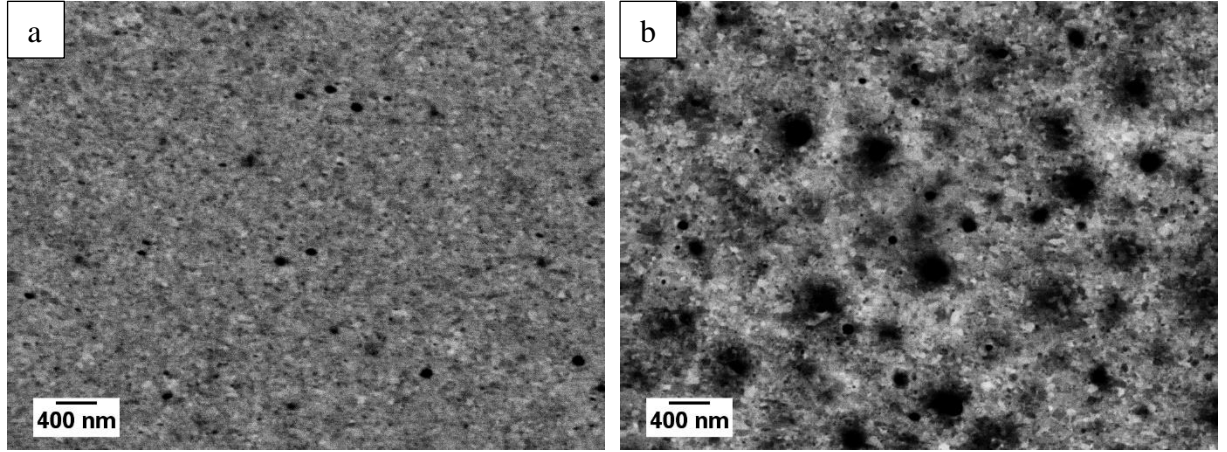
Figure 9: BSE micrographs of as-deformed $Cu_{20}Fe_{12}Co_{68}$ sample (50 revolutions at 300°C) taken at r = 3 mm: a) as-deformed b) as-deformed and CA (1h at 500°C) . The shearing direction is parallel to the horizontal axis.

The as-deformed $Cu_{20}Fe_{12}Co_{68}$ sample shows a better intermixing of phases than the as-deformed $Cu_{20}Fe_{56}Co_{24}$ sample. This can be recognized by the lower phase contrast in Figure 9 a). Residual particles (black globular shaped) occur in both as-deformed samples. Due to the BSE-contrast, elements with a lower atomic number appear darker in the micrographs. The residual particles are probably Fe or Co particles, but an exact identification is not possible because of the small difference of atomic numbers. Moreover, superimposing channeling contrast is also present. An increase of shear strain could reduce the number of residual particles. The CA caused in both compositions a grain coarsening, corresponding to the Vickers hardness measurements in Figure 6. Moreover, the annealing treatment led to a homogenization in respect of phase distribution in the entire sample. Due to diffusion processes favored by higher temperatures, a migration of grain boundaries takes places and thus the grains rearrange

15

themselves. Thus, an increase in temperature leads to an increase in grain size. The driving force behind grain coarsening is the reduction of surface energy. A small number of large grains is energetically more favorable than a high number of small grains. The CA sample in Figure 8 b) shows a complete phase separation and equally large grains. Because of the high phase contrast, the bright phases can be identified as Cu and the darker ones as Co or Fe. In comparison, the CA sample in Figure 9 b) exhibits a weaker phase contrast. Furthermore, dark regions start to form, which can be identified as Co or Fe again. The weaker phase contrast indicates that the phase separation process is still in the early stages.

3.3 Qualitative phase analysis by XRD measurements

To study the constituting crystallographic phases of $Cu_{20}Fe_{56}Co_{24}$ and $Cu_{20}Fe_{12}Co_{68}$, XRD measurements were carried out, shown in Figure 10. For this purpose, the measured XRD patterns of the compositions were compared to the calculated diffraction patterns of the individual elements: Cu-fcc, Fe-bcc, Co-hcp. However, K. Edalati et al [19] showed that HPT deformation of pure Co can effect an allotropic phase transformation of hcp to fcc when the grain size can be reduced down to the nanometer regime, so that a fcc and a distorted hcp structure coexist together, therefore Co-fcc was also taken into account as well.
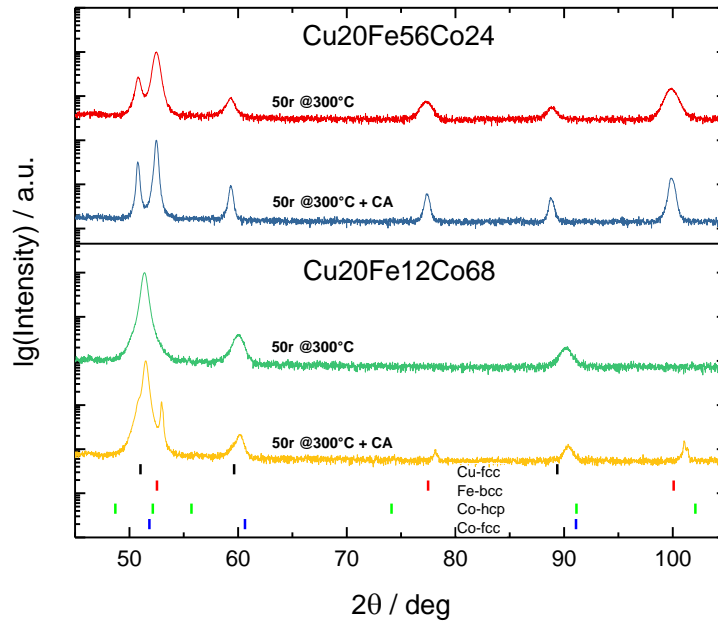
Figure 10: XRD measurements of as-deformed and subsequent annealed $Cu_{20}Fe_{56}Co_{24}$ and $Cu_{20}Fe_{12}Co_{68}$ samples. The XRD patterns were taken using Co-Kα radiation.

To resolve even small particles, a logarithmic scale of normalized intensities of measured patterns was used as a function of the Bragg angle 2θ. The measured patterns of as-deformed $Cu_{20}Fe_{12}Co_{68}$ (50 revolutions at 300°C), shown in Figure 10, exhibit mainly mixed peaks of Cu-fcc and Co-fcc, whereby the Co-hcp and Co-fcc patterns nearly overlap at Bragg angles of about 52° and 91°. It can be seen that a single phase fcc structure, consisting mainly of Co-fcc, has been obtained. There are no Fe-bcc peaks present, and therefore one can assume that Fe-bcc is dissolved in the fcc matrix. In the pattern below, showing the results of the CA sample, a phase separation took place. The additional obtained larger peaks correspond to the calculated Fe-bcc pattern at best. Moreover, a slight precipitation of Co-hcp took place in the mixed peak of Cu-Co-fcc and thus a structure consistent of three phases (bcc, fcc and hcp) resulted by the CA. Compared as-deformed $Cu_{20}Fe_{56}Co_{24}$ to as-deformed $Cu_{20}Fe_{12}Co_{68}$, the as-deformed Fe-rich specimen exhibited a lower intermixing of phases. In spite of the same processing parameters, a dual phase microstructure (Fe-bcc and Cu-Co-fcc) can be observed for $Cu_{20}Fe_{56}Co_{24}$. The intensity of the Fe-bcc peak is also higher than the mixed Cu-Co-fcc peak, which correlates with the chemical composition of the sample. A CA of as-deformed $Cu_{20}Fe_{56}Co_{24}$ resulted in a narrowing of full width at half maximum (FWHM). The same behavior, but weaker, was observed for the Co-rich composition. This indicates an increase in grain size, which is in agreement to the BSE micrographs in Figure 8 and Figure 9 according to Scherrer's law. However, the aim of this study is to obtain a microstructure with intermixed phases such as for $Cu_{20}Fe_{12}Co_{68}$ (50 revolutions at 300°C). For this purpose, a further processing step was necessary prior to HPT deformation of the $Cu_{20}Fe_{56}Co_{24}$ composition.

3.4 Influence of BM on structural evolution of $Cu_{20}Fe_{56}Co_{24}$

3.4.1 Progress on phase formation as a function of milling time

As mentioned above, the XRD-pattern of the Fe-rich sample processed by HPT deformation shows two crystallographic phases in the as-deformed state. The purpose of the following is to enhance intermixing already of the initial powder mixture by BM. Figure 11 shows the progress of phase formation and development of microstructure dependent on milling time. After 2h milling time in argon atmosphere, still a high number of peaks can be observed, corresponding to Fe-bcc, Cu-fcc and Co-hcp.
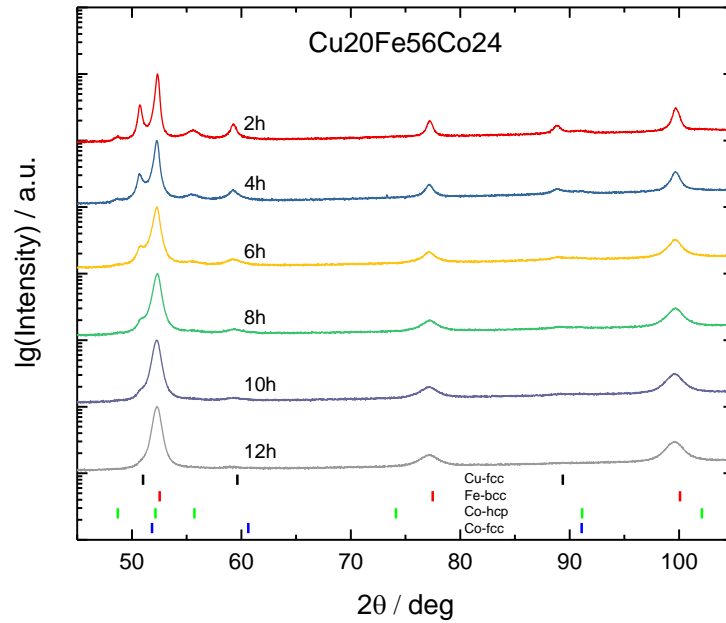
Figure 11: XRD measurements of ball milled $Cu_{20}Fe_{56}Co_{24}$ powder at various milling times. XRD patterns were taken using Co-Kα radiation.

After 6h, Co-hcp peaks disappeared almost completely and Cu-fcc peaks became significant smaller with regard to intensity. The desired microstructure has been reached after a milling time of 12h. Compared to the measured pattern after 2h, all fcc peaks vanished completely, indicating the formation of a homogenous single-phase bcc microstructure. A peak broadening, i.e. increasing FWHM, was observed for an increasing milling progress, implying grain refinement. Nevertheless, HPT pre-compaction and deformation was necessary to obtain bulk samples out of the 12 hours milled $Cu_{20}Fe_{56}Co_{24}$.

3.4.2 Effect of BM on microhardness

Next, the powder mixtures prepared by BM were used to produce a bulk sample by HPT. Figure 12 shows LM images of as-deformed $Cu_{20}Fe_{56}Co_{24}$ samples, whereby the initial powder composition was ball milled for 12h. Large stress-induced cracks can be observed in radial direction of the sample deformed at RT, shown in Figure 12 a). The unknown but extremely high applied strain by BM leads to enhanced hardness of BM powder blends. Thus, HPT deformation had to be interrupted after 5 revolutions at RT to prevent a further crack formation.

Figure 12: LM images of HPT deformed $Cu_{20}Fe_{56}Co_{24}$ sample prepared by 12h ball milling. a) 5 revolutions at RT b) 10 revolutions at 300°C c) 10 revolutions at 400°C d) 10 revolutions at 500°C.

As a consequence, processing temperature has been increased to 300°C, 400°C and 500°C during HPT (10 revolutions in each case). The resulting samples are displayed in Figure 12 b)-d). $Cu_{20}Fe_{56}Co_{24}$ deformed at 300°C exhibits more cracks than at RT, which can be explained by the double amount of applied shear strain. The crack in axial direction in c) originates from sample preparation, such as cutting and polishing. The spots in d) originate from polishing residues. As can be seen, less cracks are visible the higher the processing temperatures. All samples show a homogenous appearance in respect of microstructure and grain sizes below the resolution limit of the LM. The above-mentioned samples, excepted the sample deformed at RT, were exposed to a CA treatment.

The mean Vickers hardness and standard deviation of all investigated as-deformed and CA samples are plotted in Figure 13. To compare the effect of BM, hardness testing is carried out and compared to the hardness of HPT-deformed samples (see Figure 6). Because BM applies an undefined amount of strain onto the powders, this comparison was carried out by comparing the mean hardness, taken for $r \geq \pm 2$ mm. Basically, hardness of $Cu_{20}Fe_{12}Co_{68}$ and $Cu_{20}Fe_{56}Co_{24}$ were compared, whereby both were fabricated of ordinary powders and then deformed via HPT as described in the previous section (see yellow shaded area "HPT"). Furthermore, Figure 13 shows a plot of the mean microhardness of HPT deformed $Cu_{20}Fe_{56}Co_{24}$ samples, which were fabricated out of 12 hours ball milled powder as described in the previous section (see gray shaded area "BM+HPT"). The microhardness of conventional fabricated $Cu_{20}Fe_{12}Co_{68}$ and $Cu_{20}Fe_{56}Co_{24}$ via HPT (yellow shaded area) has been already discussed in chapter 4.2.
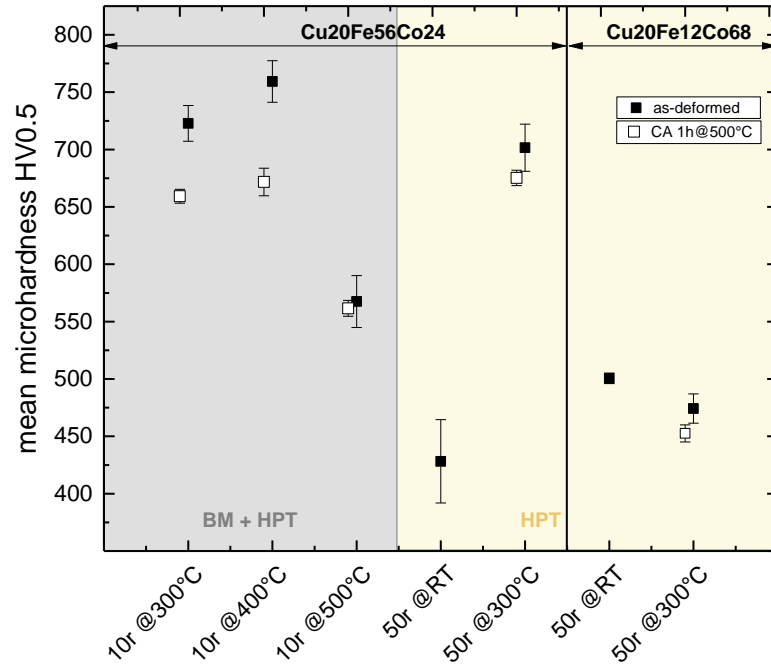
Figure 13: Mean hardness dependent on composition, method of production and processing parameters.

Deformation at higher temperatures leads to a larger grain size in the steady state. This effect can be described by grain boundary migration acting against shear-induced grain refinement. The hardness decreases generally with increasing processing temperature, however, the BM+HPT samples (each deformed by 10 revolutions) in the gray shaded area exhibit hardening for increasing deformation temperatures and reach a maximum of about 760 HV at 400°C. For comparison, a processing temperature of 300°C led to a hardness of approximately 720 HV, while a processing temperature of 500°C led to 570 HV. A similar hardening behavior was widely reported in NC metals for an annealing treatment after HPT. This hardening phenomena has been explained by solute segregation to grain boundaries and dislocation source hardening [20]. Maybe, the hardening phenomena also occurs during HPT deformation at specific processing temperatures. A further reason for the higher hardness could be the somewhat more homogenous microstructure of the sample deformed at 400°C compared to the sample deformed at 300°C (see appendix). As usual, the as-deformed samples were exposed to a CA treatment and then the hardness measured, which is also depicted in Figure 13. As can be seen, the CA had the highest influence on the sample deformed by 10 revolutions at 400°C, where the hardness decreases nearly by 100 HV. Nearly the same hardness level has been reached for $Cu_{20}Fe_{56}Co_{24}$ which was as-deformed by 10 revolutions at 300°C (BM+HPT) and by 50 revolutions at 300°C (HPT), though the BM+HPT sample fractured at several positions due to lower ductility. Table 3 shows measured Vickers hardness values of various as-deformed (and CA) $Cu_{20}Fe_{56}Co_{24}$ samples by 10 revolutions at 300°C, 400°C and 500°C along the radii. Once

more, the CA samples were quarter discs, so that only the half amount of indentations was achievable. Because of the high number of cracks in the sample deformed at 300°C, several indentations could not be performed, which is why some table fields are empty. The hardness of all samples remained almost constant along the radii.

Table 3: Vickers microhardness of 12h ball milled and then HPT deformed $Cu_{20}Fe_{56}Co_{24}$ sample at different radii r. Each sample was deformed by 10 revolutions at given processing temperatures.

r / mm	microhardness HV0.5					
	300°C	400°C	500°C	300°C+CA	400°C+CA	500°C+CA
-3.50	743	764	595			
-3.25	743	757	598			
-3.00	733	757	538			
-2.75	727	764	571			
-2.50		761	569			
-2.25		761	551			
-2.00	723	740	543			
-1.75	723	737	532			
-1.50	747	775	517			
-1.25	750	783	506			
-1.00	726	772	522			
-0.75		764	526			
-0.50		750	543			
-0.25		775	545			
0		761	565	653		
0.25		740	551	656	665	569
0.50	714	757	538	665	659	543
0.75	704	768	516	665	623	538
1.00	707	761	516	670	603	536
1.25	710	754	516	668	656	532
1.50	695	717	534	650	665	540
1.75	695	757	538	645	668	545
2.00	707	779	538	662	668	549
2.25	698	790	549	659	668	565
2.50	701	775	547	659	650	567
2.75	714	2,75	558	659	682	567
3.00	723	764	565	650	688	560
3.25	710	764	576	656	673	567
3.50	737	713	581	670	673	556

3.4.3 Structural evolution of milled and as-deformed $Cu_{20}Fe_{56}Co_{24}$

SEM-BSE micrographs were taken of the BM+HPT $Cu_{20}Fe_{56}Co_{24}$ samples at a radius of 3 mm. BM+HPT samples (10 revolutions at 300°C, 400°C and 500°C) are shown in Figure 14-16 a), respectively. Next to the as-deformed samples, the microstructure after a CA of each sample is shown in Figure 14-16 b), respectively.
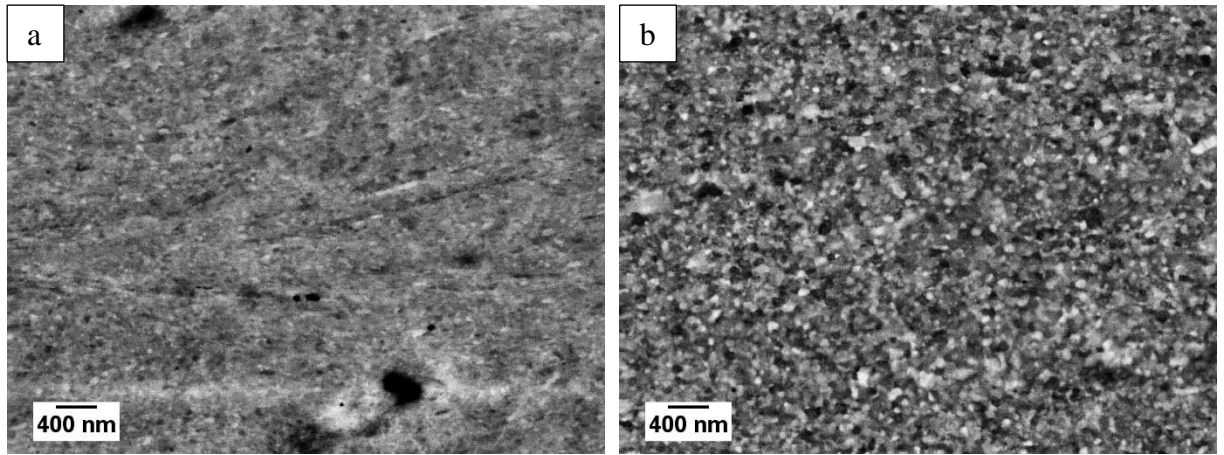
Figure 14: BSE micrographs of the $Cu_{20}Fe_{56}Co_{24}$ sample after 12h BM and HPT deformation by 10r at 300°C at r=3mm a) as-deformed b) subsequently CA.
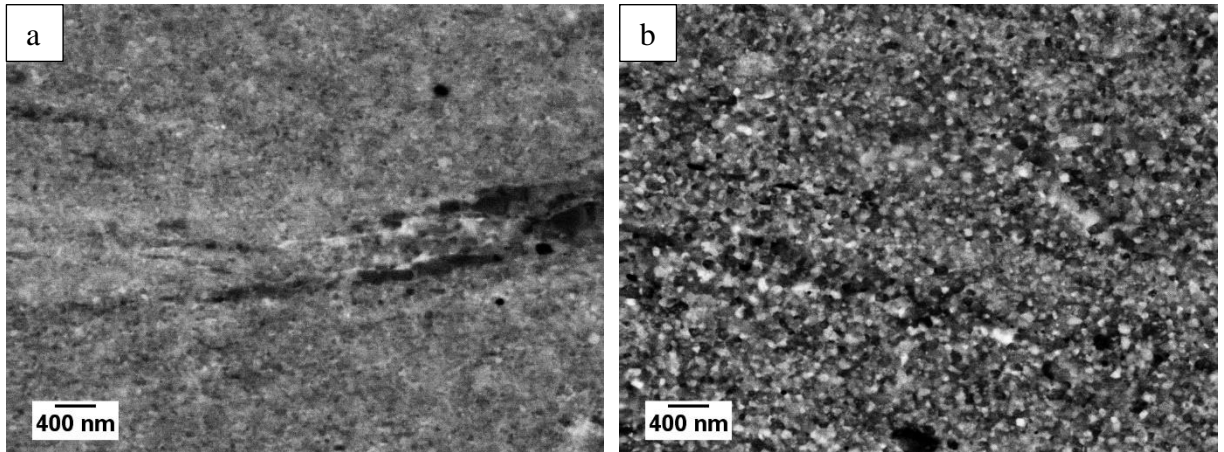
Figure 15: BSE micrographs of the $Cu_{20}Fe_{56}Co_{24}$ sample after 12h BM and HPT deformation by 10r at 400°C at r=3mm a) as-deformed b) subsequently CA.
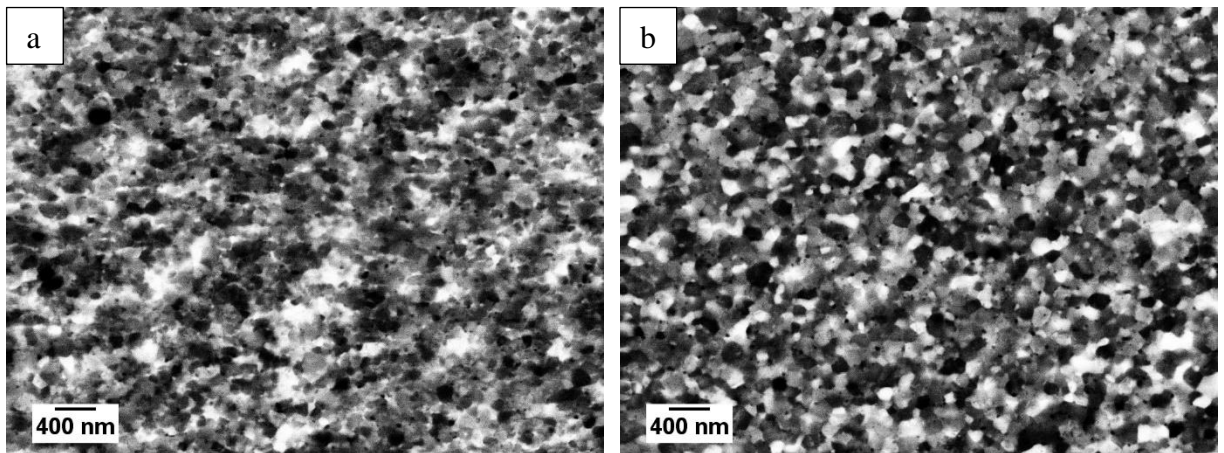
Figure 16: BSE micrographs of the $Cu_{20}Fe_{56}Co_{24}$ sample after 12h BM and HPT deformation by 10r at 500°C at r=3mm a) as-deformed b) subsequently CA.

22

Due to BM, a relative homogenous NC microstructure could be reached in all samples (see Figure 21-23 attached in appendix), even at $r = 0$ mm and $r = 1$ mm a steady state in structure and hardening could be achieved. Therefore, micrographs of Figure 14-16 a) represent the microstructure of the whole sample, respectively. Deformation at 400°C exhibited a similar microstructure than at 300°C and both have a much finer but less homogenous microstructure than at 500°C. The latter exhibits larger grains, which are in the submicron regime. Therein, also a segregation of phases can be observed, whereby the individual phases could be identified roughly. With increasing atomic number of elements, the intensity of detected signal increases, i.e. white grains are most likely Cu grains. As the difference in atomic number of Fe and Co is very small, it is not possible to distinguish clearly between these two elements. Furthermore, channeling contrast is also present. As can be seen, the individual phases arranged themselves to small clusters. No less deformed regions occurred in the sample deformed at 500°C in contrast to the samples deformed at lower temperatures. The CA had a weak influence with respect to grain size growth, nonetheless a uniform particle distribution as well as a high phase contrast could be achieved. Better results for phase mixing could be achieved for deformation temperatures at 300°C and 400°C, shown in Figure 14 a) and Figure 15 a). The NC microstructure of both appeared mainly greyish, indicating a successful phase intermixing, in contrast to the sample deformed at 500°C. In both cases the heat treatment led to phase separation and grain coarsening, especially in the less deformed regions grain size increases faster. The hardness values of BM+HPT samples (as-deformed and CA) correlate quite well with the structure observed in the BSE micrographs in Figure 14-16.

3.4.4 Qualitative phase analysis of BM+HPT samples

For more detailed information about phase formation of samples mentioned in Figure 14-16, XRD measurements have been carried out, shown in Figure 17 a). If one looks at the pattern 10r at 300°C, a weak phase separation took place in comparison to the initial powder mixture after a milling time of 12h (see Figure 11). However, a bcc single phase microstructure can be identified. At the left side of the former peak, a weak peak has been formed, which can be identified as Cu-fcc. For Bragg angles of about 60° and 90°, also positions where Cu-fcc patterns are expected to occur, a slight increase of intensity is visible. That indicates a precipitation of Cu with respect to the structure of 12h milled $Cu_{20}Fe_{56}Co_{24}$. In the measured pattern below, CA affects an increase of Cu-fcc peak intensities and a decrease of FWHM of all peaks, arising from grain growth.
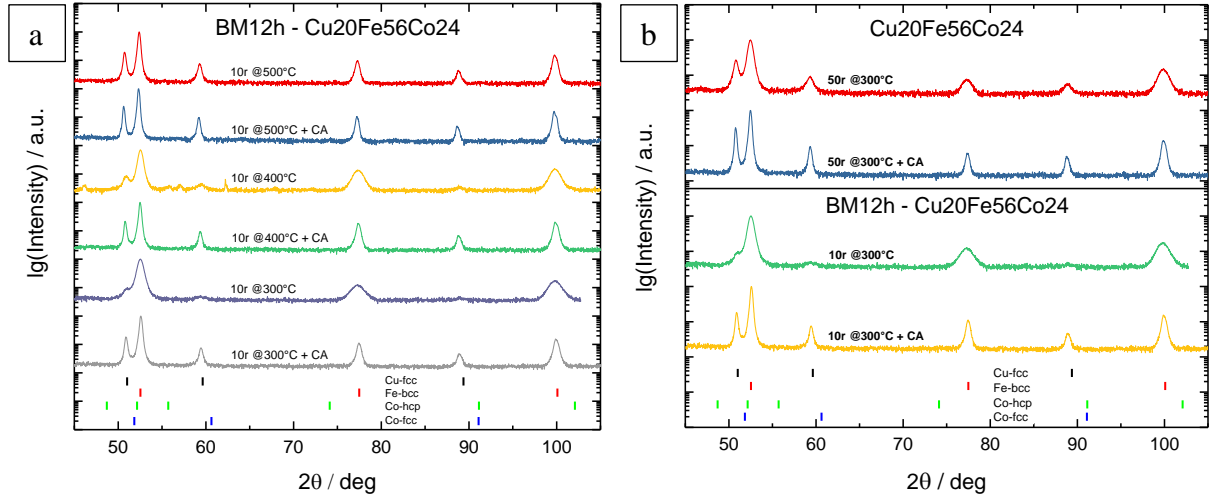
Figure 17: Measured XRD patterns of: a) $Cu_{20}Fe_{56}Co_{24}$ sample prepared by 12h BM and deformed by HPT at various processing temperatures and b) comparison of 12h BM and un-milled $Cu_{20}Fe_{56}Co_{24}$, both deformed by HPT at the same processing temperature. XRD patterns were taken using Co-Kα radiation.

The pattern after deformation at 400°C is very similar to those at 300°C, however, the detected Cu-fcc peaks are somewhat higher in intensity indicating more precipitation of Cu. There are also weak peaks, which most likely arise from oxide formation at approximately 46°, 57° and 62°. The pattern of the annealed sample (400°C+CA) is similar to the above described 300°C+CA but exhibits more intense Cu-fcc peaks. A further increase of processing temperature to 500°C had a strong influence on pattern shape. The detected peaks look sharper than at lower temperatures, i.e. higher relative intensities and narrower FWHM. By CA no evolution of any additional crystallographic phase was identified, but a peak narrowing can be observed. These patterns also correlate with the taken BSE micrographs in Figure 16.

Figure 17 b) shows a comparison of XRD measurements of as-deformed $Cu_{20}Fe_{56}Co_{24}$, whereby one sample is fabricated of a conventional powder composition ($Cu_{20}Fe_{56}Co_{24}$) and the other of a 12h ball milled composition (BM12h $Cu_{20}Fe_{56}Co_{24}$). Both variants were deformed at the same temperature, 300°C, but by a different number of revolutions. As can be seen, the sample processed by HPT only exhibits significant higher intensities for Cu-fcc peaks than the sample which was exposed to prior BM treatment. As a result, a BM process of $Cu_{20}Fe_{56}Co_{24}$ before HPT deformation leads to a better intermixing of phases. Moreover, CA of ball milled and HPT deformed samples had a smaller effect on hardness.

24

4 Conclusion and Outlook

In the framework of this study, the microstructural evolution of $Cu_{20}Fe_{12}Co_{68}$ and $Cu_{20}Fe_{56}Co_{24}$ processed by HPT deformation at different processing temperatures were investigated. In addition, the influence of BM on phase formation of $Cu_{20}Fe_{56}Co_{24}$ was studied. Moreover, all as-deformed samples were exposed to a subsequent isothermal CA treatment and compared. For this purpose, LM, SEM, Vickers hardness measurements and XRD measurements were carried out. This leads to the following conclusions:

All as-deformed samples reached a NC microstructure. Correlating XRD measurements to SEM micrographs leads to the result, that a fcc single-phase structure could be formed successfully for HPT deformed $Cu_{20}Fe_{12}Co_{68}$. A crystallographic bcc as well as fcc structure in the as-deformed state was obtained for the Fe-rich sample, $Cu_{20}Fe_{56}Co_{24}$, which was processed in the same way. A steady state in structure occurs for higher radii ($r \geq 2$ mm) in both cases.

To enhance intermixing, the powder mixtures were exposed to a BM treatment and a subsequent HPT deformation. Phase analysis of ball milled powder mixtures shows a complete intermixing of phases after a milling time of 12h leading to a bcc single-phase structure of the powder mixture. Due to an enhanced hardness induced by BM, a further application of shear strain by HPT leads to brittle samples and a significant higher number of cracks in the sample. In addition, less deformed regions are present in the entire cross-section. Nevertheless, a better intermixing of phases has been achieved for BM+HPT $Cu_{20}Fe_{56}Co_{24}$ samples in comparison. Thus, the intermixing of phases was enhanced by initial BM.

The subsequent CA of as-deformed samples leads in each sample to a grain coarsening and homogenization of the microstructure. Thus, a significant phase separation and a decrease in microhardness took place in each case. The drop of microhardness due to CA is higher for samples processed by BM and HPT.

Vickers microhardness of HPT deformed $Cu_{20}Fe_{56}Co_{24}$ sample is higher compared to HPT deformed $Cu_{20}Fe_{12}Co_{68}$ sample. Initial BM increases the hardness. Furthermore, a hardening effect by increasing the processing temperature during HPT was observed.

In further investigations, the as-deformed samples of both compositions will be used to carry out magnetization experiments. For this purpose, a ring has to be fabricated out of the sample, which functions as core for a toroidal coil. Higher shear strains by applying 100 revolutions instead 50 could reduce the size of the less deformed area in the center of the sample.

Figures

Tables

References

[1]   C. L. Chien, S. H. Liou, G. Xiao, and M. A. Gatzke, "Magnetic Percolation in New Crystalline FCC Fe-Cu Alloys," *MRS Proc.*, vol. 80, p. 395, 1986.

[2]   J. R. Childress and C. L. Chien, "Reentrant magnetic behavior in fcc Co-Cu alloys," *Phys. Rev. B*, vol. 43, no. 10, pp. 8089–8093, Apr. 1991.

[3]   G. Herzer, "Modern soft magnets: Amorphous and nanocrystalline materials," *Acta Materialia*, vol. 61, no. 3, pp. 718–734, Feb. 2013.

[4]   K. S. Kormout, R. Pippan, and A. Bachmaier, "Deformation-Induced Supersaturation in Immiscible Material Systems during High-Pressure Torsion: Deformation-Induced Supersaturation," *Adv. Eng. Mater.*, vol. 19, no. 4, p. 1600675, Apr. 2017.

[5]   O. Madelung, Ed., *Ca-Cd – Co-Zr*, vol. c. Berlin/Heidelberg: Springer-Verlag, 1993.

[6]   O. Madelung, Ed., *Cr-Cs – Cu-Zr*, vol. 5d. Berlin/Heidelberg: Springer-Verlag, 1994.

[7]   X. Fan *et al.*, "Magnetic properties of Co-Cu metastable solid solution alloys," *Phys. Rev. B*, vol. 69, no. 9, p. 094432, Mar. 2004.

[8]   R. Lardé and J. M. Le Breton, "Influence of the milling conditions on the magnetoresistive properties of a Cu80(Fe0.7Co0.3)20 granular alloy elaborated by mechanical alloying," *Journal of Magnetism and Magnetic Materials*, vol. 290–291, pp. 1120–1122, Apr. 2005.

[9]   M. Sopicka-Lizer, Ed., *High-energy ball milling: mechanochemical processing of nanopowders*. Boca Raton: CRC Press, 2010.

[10]   J. Eckert, J. C. Holzer, C. E. Krill, and W. L. Johnson, "Mechanically driven alloying and grain size changes in nanocrystalline Fe-Cu powders," *Journal of Applied Physics*, vol. 73, no. 6, pp. 2794–2802, Mar. 1993.

[11]   R. Pippan, S. Scheriau, A. Taylor, M. Hafok, A. Hohenwarter, and A. Bachmaier, "Saturation of Fragmentation During Severe Plastic Deformation," *Annu. Rev. Mater. Res.*, vol. 40, no. 1, pp. 319–343, Jun. 2010.

[12]   "ultra fine grained steel, UFG steel, carbon, strength, UTS, ductility, welding, EBSD, texture, GND, RVE, modeling, processing." [Online]. Available: http://www.dierk-raabe.com/ultrafine-grained-steels/. [Accessed: 25-Jul-2019].

[13]   R. Pippan, F. Wetscher, M. Hafok, A. Vorhauer, and I. Sabirov, "The Limits of Refinement by Severe Plastic Deformation," *Adv. Eng. Mater.*, vol. 8, no. 11, pp. 1046–1056, Nov. 2006.

[14]   A. Hohenwarter, A. Bachmaier, B. Gludovatz, S. Scheriau, and R. Pippan, "Technical parameters affecting grain refinement by high pressure torsion," *IJMR*, vol. 100, no. 12, pp. 1653–1661, Dec. 2009.

[15]   A. Bachmaier and R. Pippan*, "Generation of metallic nanocomposites by severe plastic deformation," *International Materials Reviews*, vol. 58, no. 1, pp. 41–62, Jan. 2013.

[16]   O. Renk and R. Pippan, "Saturation of Grain Refinement during Severe Plastic Deformation of Single Phase Materials: Reconsiderations, Current Status and Open Questions," *Mater. Trans.*, vol. 60, no. 7, pp. 1270–1282, Jul. 2019.

[17]   G. Gottstein, Ed., "Mechanische Eigenschaften," in *Physikalische Grundlagen der Materialkunde*, Berlin, Heidelberg: Springer Berlin Heidelberg, 2007, pp. 197–301.

[18]   "Hardnesses of the elements (data page)," *Wikipedia*. 26-Aug-2019.

[19]   K. Edalati, S. Toh, M. Arita, M. Watanabe, and Z. Horita, "High-pressure torsion of pure cobalt: hcp-fcc phase transformations and twinning during severe plastic deformation," *Appl. Phys. Lett.*, vol. 102, no. 18, p. 181902, May 2013.

[20]   O. Renk, A. Hohenwarter, K. Eder, K. S. Kormout, J. M. Cairney, and R. Pippan, "Increasing the strength of nanocrystalline steels by annealing: Is segregation necessary?" *Scripta Materialia*, vol. 95, pp. 27–30, Jan. 2015.
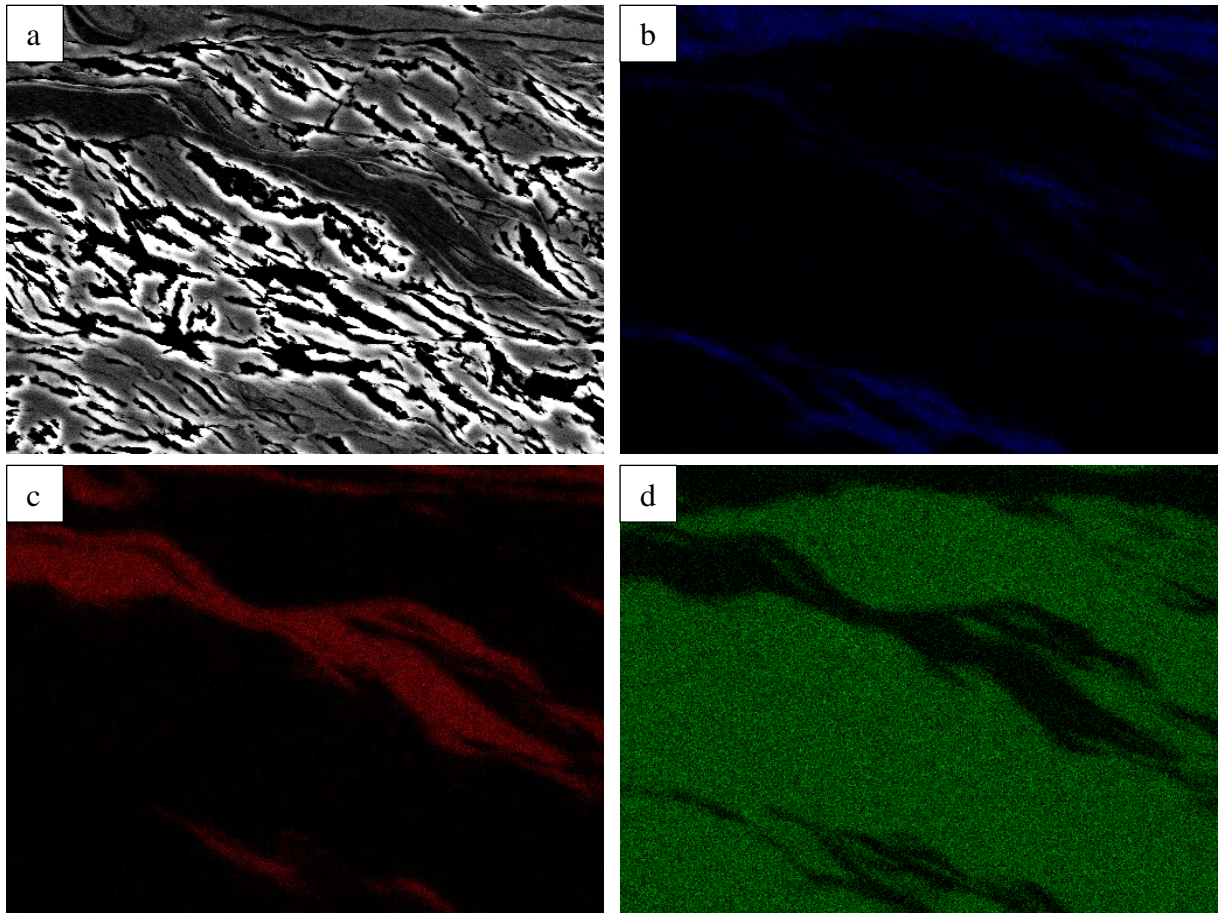
Appendix

Figure 18: a) SEM micrograph of as-deformed $Cu_{20}Fe_{12}Co_{68}$ sample (50 revolutions at RT) at a radius of 0 mm and the corresponding EDX maps of b) Cu c) Fe and d) Co. The undeformed powder mixture exhibits a chemical composition consisting of 18 at% Cu, 9 at% Fe and 73 at% Co.
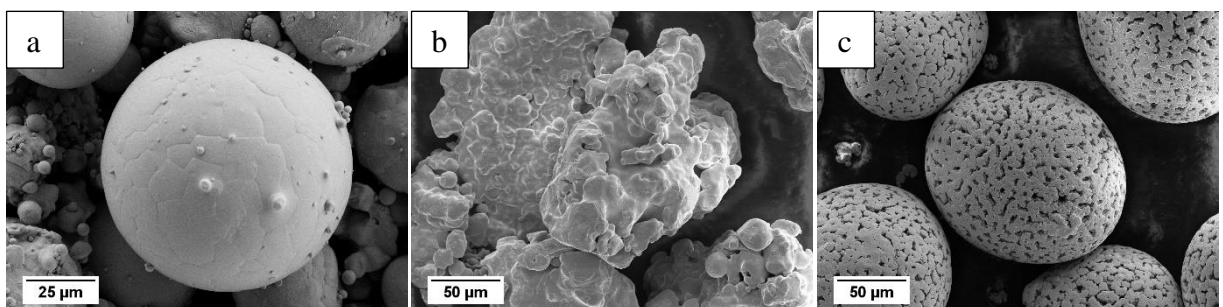
Figure 19: SEM micrographs of used initial powders: a) Cu, b) Fe and c) Co.

The following BSE micrographs show the structural evolution of as-deformed samples at given processing parameters. All micrographs were taken at the same magnification at a radius of a) 0 mm b) 1 mm c) 2 mm and d) 3 mm.
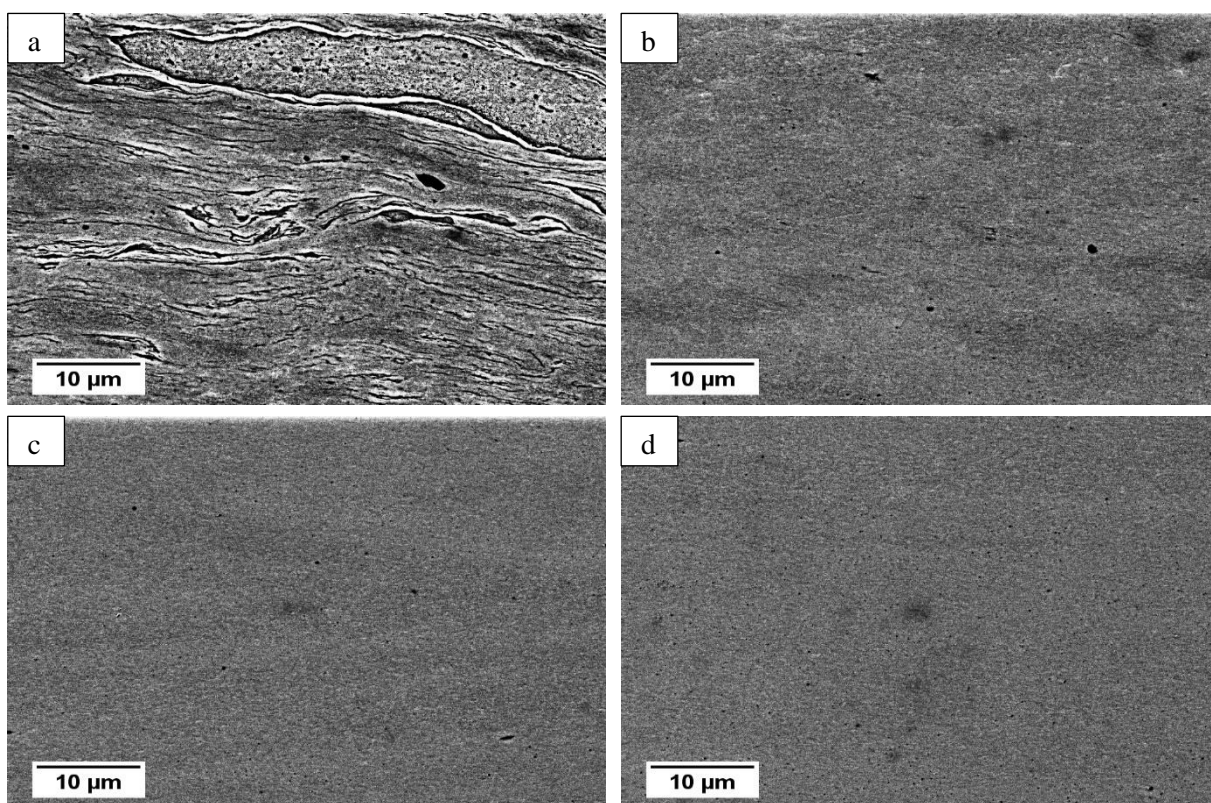
Figure 20: HPT deformed $Cu_{20}Fe_{56}Co_{24}$ sample (50 revolutions at 300°C).
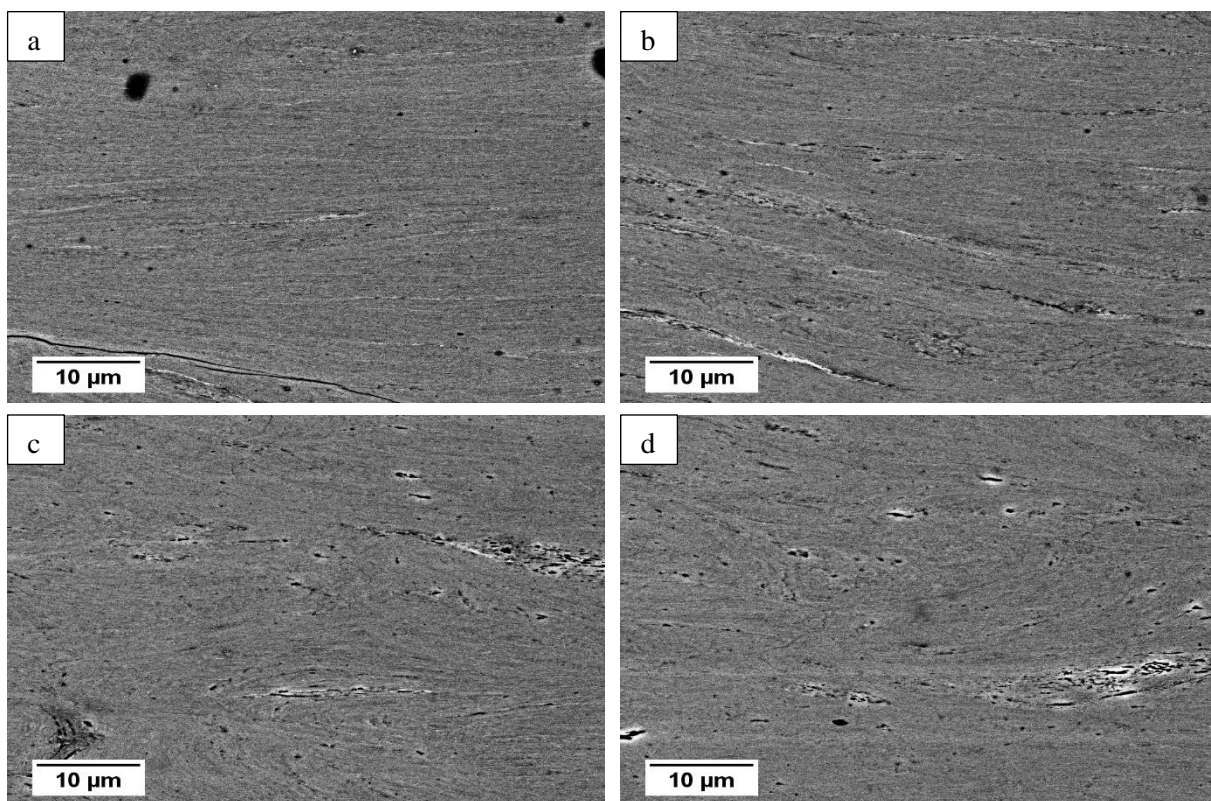

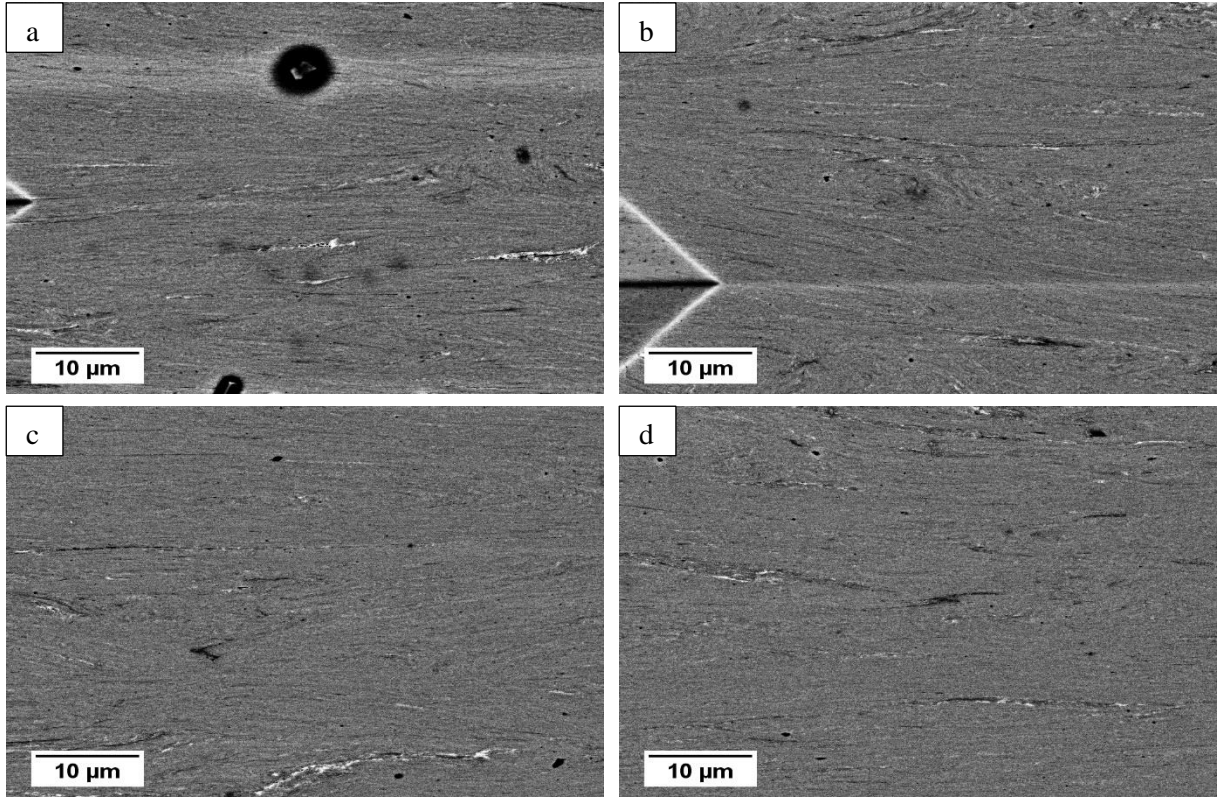Figure 21: 12h milled, then HPT deformed $Cu_{20}Fe_{56}Co_{24}$ sample (10 revolutions at 300°C).

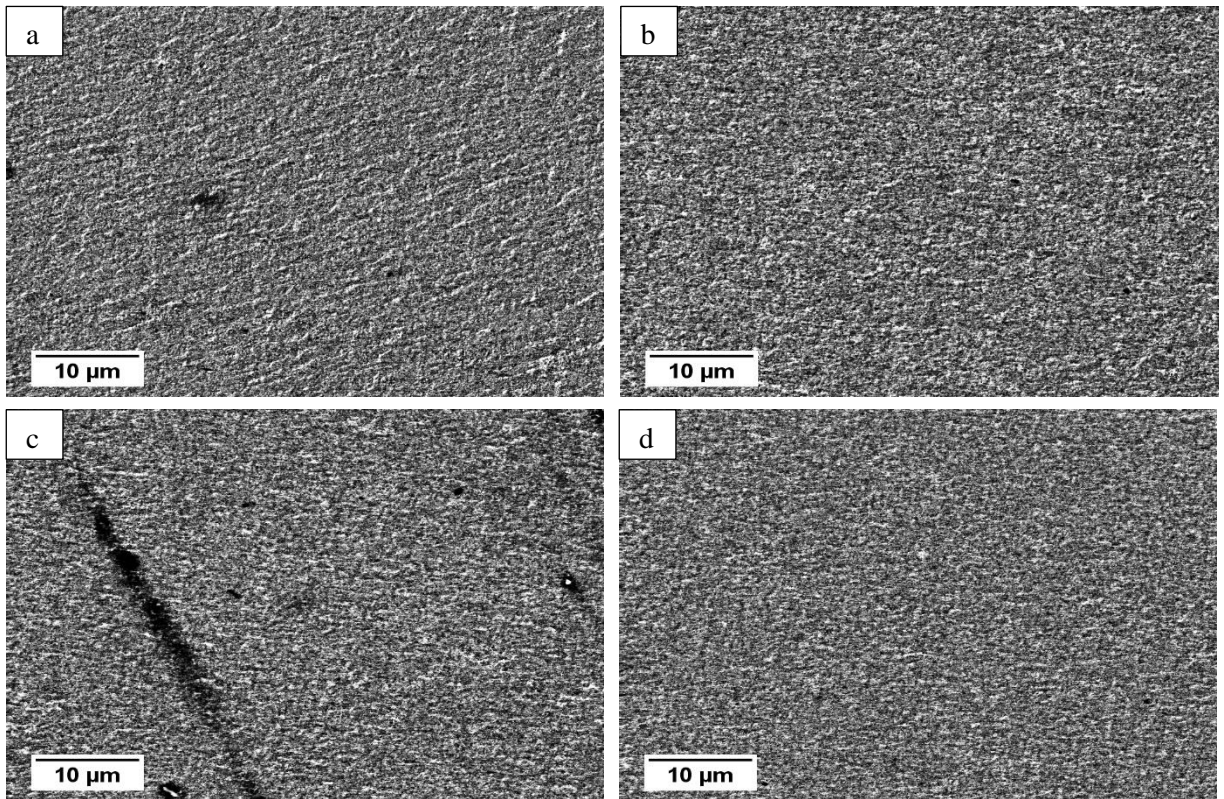Figure 22: 12h milled, then HPT deformed $Cu_{20}Fe_{56}Co_{24}$ sample (10 revolutions at 400°C).

Figure 23: 12h milled, then HPT deformed $Cu_{20}Fe_{56}Co_{24}$ sample (10 revolutions at 500°C).